

Reconstruction of attosecond beating by interference of two-photon transitions in bulk solids

Álvaro Jiménez-Galán^{1,5}, Rui E.F. Silva² & Misha Ivanov^{1,3,4}

¹*Max-Born-Institute, Max-Born Straße 2A, D-12489 Berlin, Germany.*

²*Dpto. Física Teórica de la Materia Condensada, Universidad Autónoma de Madrid, 28049 Madrid, Spain.*

³*Department of Physics, Humboldt University, Newtonstraße 15, D-12489 Berlin, Germany.*

⁴*Department of Physics, Imperial College London, South Kensington Campus, SW7 2AZ London, United Kingdom.*

⁵*jimenez@mbi-berlin.de*

The reconstruction of attosecond beating by interference of two-photon transitions (RABBIT) is one of the most widely used techniques for resolving ultrafast electronic dynamics in atomic and molecular systems. As it relies on the interference of photo-electrons in vacuum, similar interference has never been contemplated in the bulk of crystals. Here we show that the interference of two-photon transitions can be recorded directly in the bulk of solids and read out with standard angle-resolved photo-emission spectroscopy. The phase of the RABBIT beating in the photoelectron spectra coming from the bulk of solids is sensitive to the relative phase of the Berry connection between bands and it experiences a shift of π as one of the quantum paths crosses a band. For resonant interband transitions, the amplitude of the RABBIT oscillation decays as the pump and probe pulses are separated in time due

to electronic decoherence, providing a simple interferometric method to extract dephasing times.

1 Introduction

Advances in ultrafast laser technology during the last two decades have given rise to the field of attosecond science - the study and control of electron dynamics at their natural (attosecond) timescale ^{1,2}. Among the experimental techniques that made this possible, the reconstruction of attosecond beating by interference of two photon transitions (RABBIT) stands out ³⁻⁸. Since it uses weak electric fields, it allows one to monitor coherent electronic dynamics that are barely modified by the laser. RABBIT relies on the controlled interference of quantum paths in a pump-probe scheme. It can be implemented with any combination of four frequencies provided the two-photon paths created by the sequential absorption/stimulated emission of the frequencies reach the same final energy (see Methods). But, while it is in principle possible to phase-lock four different frequencies, e.g., using a signal and an idler independently to generate high harmonics, it is still technically challenging.

In its usual implementation, the quantum paths are created by two harmonics $(2N \pm 1)\omega$ of a frequency comb (the pump) that photo-ionize an initial bound electronic state (Fig. 1a). The harmonic comb is generated using a strong fundamental field of frequency ω on an inversion symmetric target, thus guaranteeing that no even $(2N\omega)$ harmonics are present. The interference of the paths containing the $(2N \pm 1)\omega$ photons is controlled by time-delaying a weak, phase-locked replica of the generating ω field (the probe) that creates sidebands at $\Omega = 2N\omega$ energies whose

intensity oscillates as a function of the pump-probe time delay τ ^{3,5,9},

$$I_{\text{SB}}(\Omega) = |A_{2N+1}(\Omega)|^2 + |A_{2N-1}(\Omega)|^2 + 2|A_{2N+1}(\Omega)||A_{2N-1}(\Omega)| \cos(2\omega\tau + \theta). \quad (1)$$

The equation above is the characteristic equation of RABBIT, computed using second-order perturbation theory, where $|A_{2N\pm 1}|$ is the absolute value of the two-photon transition amplitude from the initial state to the sideband that contains the absorption of the $2N \pm 1$ harmonic (see Methods). We use atomic unit throughout unless otherwise stated. Eq. 1 relates the measured observable, i.e., the sideband beating frequency 2ω and its phase $\theta = \Delta\phi + \Delta\varphi$, to the phase difference between adjacent harmonics in the comb, $\Delta\phi = \phi_{2N-1} - \phi_{2N+1}$, and the so-called atomic phase $\Delta\varphi$. For long pulses, the latter corresponds to the relative phase of the two-photon matrix elements^{9,10},

$$\Delta\varphi = \varphi_{2N+1} - \varphi_{2N-1} \quad (2)$$

$$= \arg \{ \mathcal{M}_{nm}((2N+1)\omega) + \mathcal{M}_{nm}(-\omega) \} - \arg \{ \mathcal{M}_{nm}((2N-1)\omega) + \mathcal{M}_{nm}(\omega) \},$$

where $\mathcal{M}_{nm}(\omega) = \sum_j \mathcal{O}_{nj} \mathcal{O}_{jm} / (E_m + \omega - E_j)$ is the two-photon matrix element, \mathcal{O}_{nm} is the dipole operator, e.g., $\mathcal{O}_{nm} = \langle n | \mathbf{r} | m \rangle$ in the length gauge, and E_m is the energy of the initial state. Initially, RABBIT was applied to characterize the relative phases of harmonics in attosecond pulse trains by assuming that the atomic phase is a smooth function of energy⁵. Later, the application of RABBIT shifted towards the reconstruction of the relative amplitudes and phases of photoionization matrix elements from different orbitals, including transitions through autoionizing states^{6,10-14}. This has allowed to extract photo-ionization time delays and reconstruct the temporal evolution of correlated electronic wavepackets^{7,15} - two hallmarks of attosecond science.

In the last decade, attosecond science has advanced from atomic and molecular targets towards condensed matter systems¹⁶. Techniques such as high harmonic spectroscopy¹⁷, high side-

band generation ¹⁸, attosecond streaking ^{19,20} and x-ray absorption spectroscopy ^{21,22} have been implemented in solids, allowing e.g., to image valence potentials with picometer resolution ²³, track metal-to-insulator ²⁴ and topological phase transitions ^{25,26}, characterize inelastic scattering time in dielectrics ²⁷, or control and measure the valley degree of freedom ^{18,28}. The RABBIT technique has been recently used to perform time-resolved photoemission experiments from solid surfaces, i.e., surface RABBIT ^{29,30}, where the time delay of electrons emitted from noble gas surfaces to the photoionization continuum was extracted.

The RABBIT technique has not yet been applied to study dynamics in the bulk of solids, i.e., transitions between bands. One of the reasons is that the interference of the two-photon paths occurs in the photo-electron continuum. The other is that, due to the spacing of lower conduction bands at each crystal momenta, the standard $[(2N \pm 1)\omega \mp \omega]$ configuration would need to rely on virtual transitions between bands, leading to a weak signal.

Here, we show that the first problem can be solved by using standard angle-resolved photoemission spectroscopy (ARPES). For the second problem, rather than relying on virtual transitions, we show that we can take advantage of resonant interband transitions, similar to resonant transitions between autoionizing states in atoms, where the RABBIT signal is strong. We demonstrate that the phase of the RABBIT beating in bulk solids allows to record information on the relative phase of the Berry connections between the bands. As in atoms, this may allow to extract excitation time delays associated with interband transitions. Akin to transitions between autoionizing resonances in atoms, the RABBIT beating in solids remains even when the pump and probe pulses

do not overlap in time. In contrast to autoionizing atomic systems, however, the decay of the beating in crystals is dominated by electronic dephasing. We thus show that \mathbf{k} -resolved decoherence times in solids can be reconstructed by tracking the decay of the RABBIT beating as a function of the pump-probe time delay.

2 Results

In atoms and molecules, RABBIT has been applied for transitions between atomic bound states and the photoionization continuum. In solids, analogies to this case can be drawn for transitions between deep valence bands, which display a flat dispersion relation, and high conduction bands, where the fine band spacing can be considered as a continuum at a given crystal momentum \mathbf{k} . Due to the computational cost of simulating a large number of high-lying bands, we will not consider such processes in this work. Here, we will concentrate on extracting dynamical information of transitions between bands that are close to the gap of semiconductor materials. At each crystal momenta \mathbf{k} , the energy separation between these bands is usually larger than typical mid-IR laser frequencies used for time-resolved spectroscopy in solids. Therefore, we distinguish two cases: transitions through virtual and resonant intermediate states.

Let us illustrate first the case of virtual intermediate states. For this, we consider a two-band model of hexagonal boron nitride, where we include only one valence and one conduction band (Fig. 1b). The band structure and dipole couplings are calculated from first principles (see Methods). We perform a RABBIT measurement using a fundamental probe field of $\lambda \approx 2.9 \mu\text{m}$

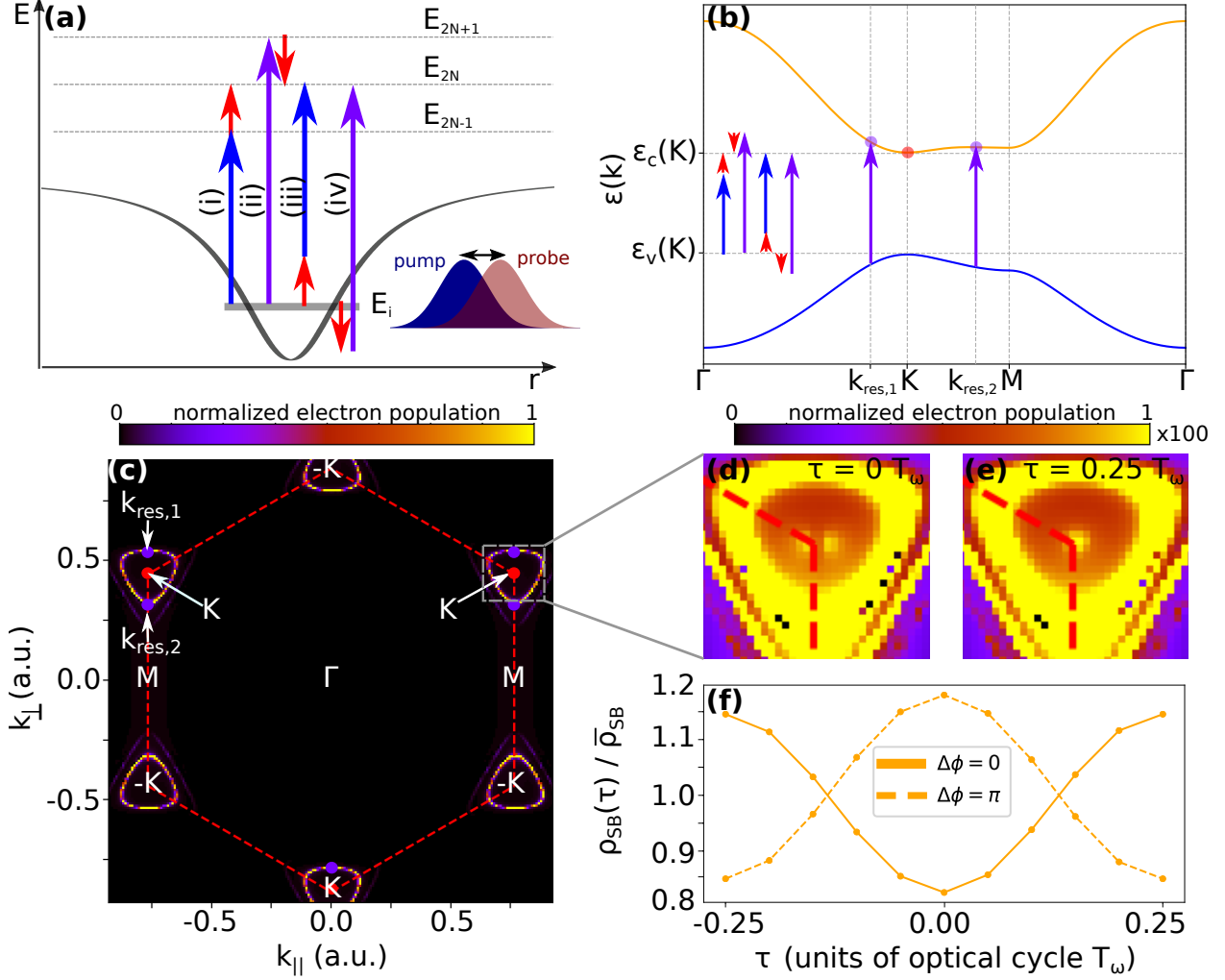


Figure 1: (a) The RABBIT scheme for an isolated atom with one electronic bound state with energy E_i and a smooth continuum. Four paths contribute to the RABBIT signal at the sideband energy E_{2N} . The $(2N + 1)\omega / (2N - 1)\omega$ photons are colored purple / blue, and the ω photons are colored red. The pump $((2N \pm 1)\omega)$ and probe (ω) pulses are delayed a time τ . (b) The virtual RABBIT scheme in k space in hBN. The sideband signal is observed at \mathbf{K} (red dot), where the energy dispersion of the conduction and valence bands satisfy $\varepsilon_c(\mathbf{K}) - \varepsilon_v(\mathbf{K}) = 2N\omega$. In addition, along this k -path, the $(2N + 1)\omega$ photon resonantly couples the valence and conduction bands at two crystal momenta \mathbf{k}_{res} (purple dots). (c) Electron momentum distribution in the conduction band's first Brillouin zone (red dashed hexagon) after the pulses for $\tau = 0$. The signal at all the \mathbf{k}_{res} dominates. (d) Zoom-in of the region close to the sideband crystal momentum \mathbf{K} (red dot at the vertex of red hexagon), with the resolution enhanced 100 times. (e) Same as (d) at $\tau = 0.25T_\omega$, with $T_\omega = 2\pi/\omega$. (f) Sideband population ρ_{SB} as a function of τ , normalized to the average population $\bar{\rho}_{SB} = \sum_{N_\tau} \rho_{SB}(\tau_{N_\tau})/N_\tau$, with N_τ the number of time delays considered. The phase of the oscillation changes by π as the harmonic phase $\Delta\phi$ changes by π .

and its 13th and 15th harmonic as the pump. The field strength of the fundamental is $F_\omega = 0.08 \text{ V/\AA}$, while that of the harmonics is $F_{13\omega} = F_{15\omega} = 0.001 \text{ V/\AA}$. The fields are kept weak to minimize intraband transitions and ensure a perturbative process where Eq. 1 is valid. Their duration is 100 fs and they are polarized along the Γ - \mathbf{M} direction of the crystal (Fig. 1(b,c)). The lower harmonic photon lies below the minimum band gap. In contrast, the upper harmonic photon resonantly couples the valence and conduction bands at the crystal momenta satisfying $\varepsilon_c(\mathbf{k}_{\text{res}}) - \varepsilon_v(\mathbf{k}_{\text{res}}) = (2N + 1)\omega$, with $\varepsilon_{c/v}(\mathbf{k})$ the dispersion of the conduction/valence band. In Fig. 1b we show two of this resonant momenta along the path Γ - \mathbf{K} - \mathbf{M} - Γ (purple dots). At the crystal momenta \mathbf{K} , a sideband at energy $\varepsilon_c(\mathbf{K}) - \varepsilon_v(\mathbf{K}) = 14\omega$ is populated via the two-photon processes characteristic of RABBIT through virtual intermediate states (Fig. 1b). In the weak field regime, the vector potential is small and thus intraband currents can be neglected. Therefore, the conduction band will be populated at the resonant momenta \mathbf{k}_{res} , and at the sideband momentum \mathbf{K} . The latter should oscillate as a function of the pump-probe time delay τ according to Eq. 1.

Fig 1c shows the electron momentum distributions in the conduction band's first Brillouin zone after the interaction with the fields for a pump-probe time delay $\tau = 0$. This observable can be obtained, as it is done in ARPES, via the photoelectric effect. The signal is dominated by the electron population at the one-photon resonant momenta \mathbf{k}_{res} . The sideband signal at \mathbf{K} is not visible in this scale, highlighting the key problem of the non-resonant scheme: the sideband signal, coming from two-photon virtual transitions, is too weak compared to the one-photon resonant signal. In this case, the sideband signal can only be extracted with exquisite resolution.

For the sake of argument, let us assume such high resolution is possible. Fig. 1(d,e) show a zoom-in of \mathbf{K} for two pump-probe time delays $\tau = 0$ and $\tau = \pi/(2\omega)$, whose separation is half the RABBIT period (one quarter optical cycle). The signal is enhanced 100 times with respect to panel (c). Exactly at \mathbf{K} (vertex of the red dashed line), there is a population minimum for $\tau = 0$ and a maximum for $\tau = \pi/(2\omega)$, indicating opposite path interference in accordance with the RABBIT mechanism. Fig. 1f shows the sideband signal, i.e., electron population at \mathbf{K} , for several pump-probe time delays spanning one RABBIT period. The sideband population oscillates with the RABBIT frequency 2ω (Eq. 1). The solid and dashed curves are calculated with the same laser parameters except for the phase difference between the two harmonics $\Delta\phi$. For the solid curve, $\Delta\phi = 0$, while for the dashed curve $\Delta\phi = \pi$. The π difference in the harmonic phase is recorded in the RABBIT oscillation phase, in accord with Eq. 1.

We now turn to the case of resonant intermediate transitions. Here, the standard RABBIT scheme involving $(2N \pm 1)\omega$ and ω photons requires three conduction bands separated by ω at a given sideband momentum \mathbf{k}_{SB} . In the case that four independent phase-locked frequencies were available, there would be no constraints. However, since producing the latter is experimentally challenging, below we show that it is not hard to find a crystal momentum where the standard scheme would work for typical laser frequencies.

Fig. 2a shows the band structure of hBN along the \mathbf{K} - \mathbf{M} direction, where we have now included also the six sp_2 orbitals, which are the next closest in energy. At the crystal momentum \mathbf{k}_{SB} , where the blue and red arrows are located in Fig. 2a, the sp_2 conduction bands are separated

by roughly the third harmonic of a standard Ti:Sapph laser, $\lambda \approx 270$ nm. We use this system as an example to illustrate the resonant RABBIT technique in the bulk of solids.

We use the fundamental frequency $\omega = 0.167$ a.u., corresponding to $\lambda = 270$ nm (3rd harmonic of Ti:Sapph), and its 7th and 9th harmonic. The harmonics are resonant with the lowest and highest sp_2 conduction bands from the lowest sp_2 valence band at \mathbf{k}_{SB} (blue and purple arrows in Fig. 2a). The time-delayed probe, carried at ω , is resonant with the intermediate sp_2 band (the sideband, orange curve in Fig. 2a) from the other two sp_2 conduction bands at \mathbf{k}_{SB} . Since all the valence bands are fully occupied before the pump photon arrives, the dynamics are triggered by it. Hence, the sideband is populated predominantly via two quantum paths: (i) by the absorption of a 7ω photon, followed by the absorption of a ω photon, (ii) by the absorption of a 9ω photon, followed by the stimulated emission of a ω photon (Fig. 2a). The pump fields have a strength of $F_{7\omega} = F_{9\omega} = 0.01$ V/Å and we choose a relative phase of $\phi_{9\omega} - \phi_{7\omega} = \pi$. The probe pulse has a strength $F_{\omega} = 0.02$ V/Å. All fields are 15 fs long and linearly polarized along the \mathbf{K} - \mathbf{M} direction.

In Fig. 2b,c we show the \mathbf{k} -resolved electron population of the sideband in a slice of the first Brillouin zone along the \mathbf{K} - \mathbf{M} direction for two time delays separated by half the RABBIT period. The sideband momentum \mathbf{k}_{SB} is encircled by the dashed white line and shows maximum electron population for panel (b) and a minimum for panel (c). In contrast to the case of virtual transitions, the sideband signal is now not masked by neighbouring signals and is clearly visible. Fig. 2d shows the sideband electron population integrated inside the white dashed circle for several pump-probe time delays displaying the characteristic RABBIT oscillation frequency.

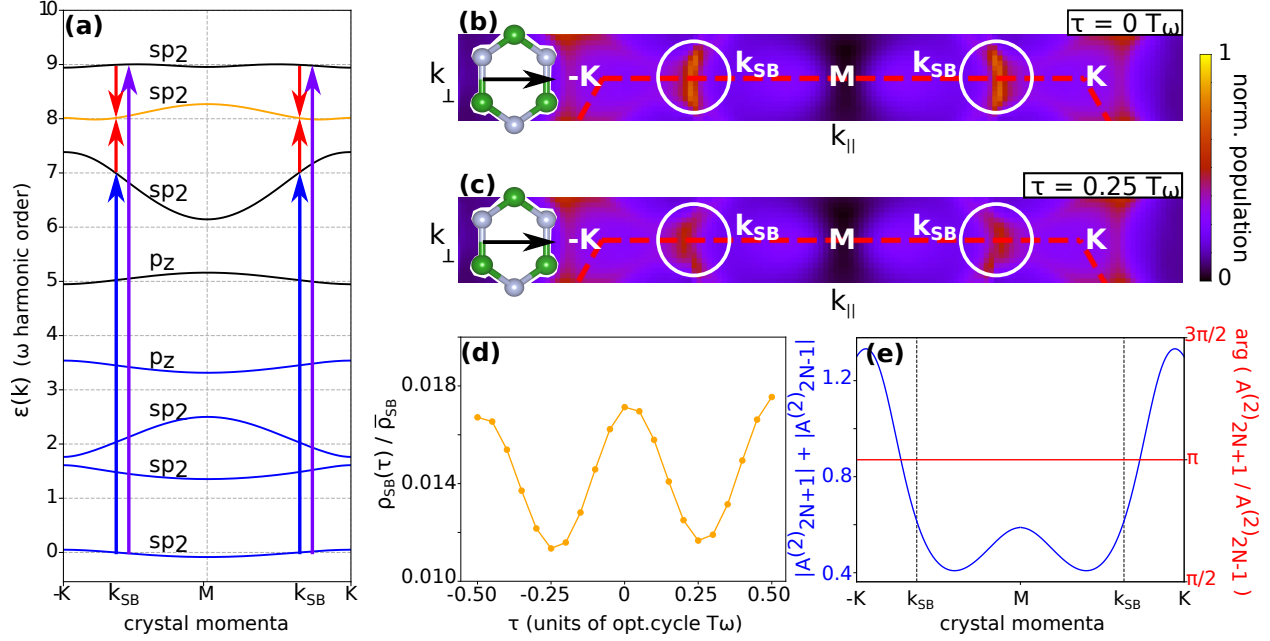


Figure 2: (a) Energy dispersion of hBN. The vertical axis is in units of the fundamental frequency $\omega = 0.167$ a.u. Blue/purple arrows indicate absorption of a pump photon $7\omega/9\omega$, while red arrows indicate absorption/stimulated emission of a probe photon ω , which is delayed by a time τ . The RABBIT beating is measured at k_{SB} . (b,c) Electron momentum distribution of the sideband (orange curve in (a)) along the $\mathbf{K} - \mathbf{M}$ ($k_{||}$) direction for a pump-probe time delay of (b) $\tau = 0$ and (c) $\tau = 0.25 \omega$ -cycles. The k_{SB} momenta is enclosed by white circles and the red-dashed line indicates the edges of the first Brillouin zone. The top left inset shows the hBN lattice with the black arrow indicating the polarization of the laser fields ($||$ direction). (d) Normalized population of the sideband in the region delimited by the white circles in (b,c) as a function of τ , displaying the RABBIT beating. (e) Amplitude (blue, left axis) and phase (red, right axis) of the two-photon Berry connections (see text for details). The black dotted lines indicate k_{SB} .

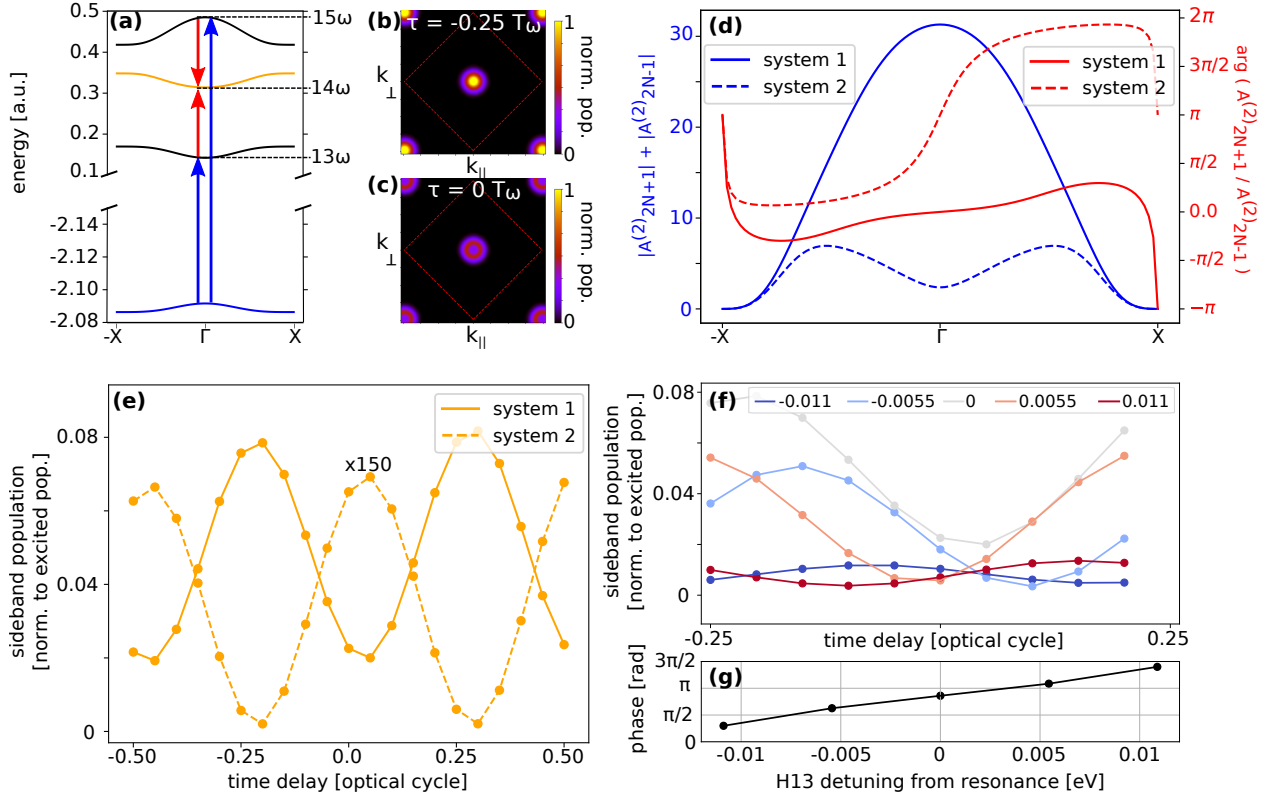


Figure 3: RABBIT phase dependence on the atomic phase. (a) Band structure of model systems 1 and 2. The RABBIT scheme is performed at the Γ point, with $\omega = 0.172$ a.u., $F_{13\omega} = F_{15\omega} = 0.05$ GV/m, $F_{\omega} = 0.1$ GV/m and 20 fs full width half maximum duration. (b,c) Electron momentum distributions in system 1 for two different time delays. The red dashed rhombus indicates the edges of the first Brillouin zone, while the center corresponds to the Γ point. (d) Amplitude (blue curves, left axis) and phase (red curves, right axis) of the two-photon Berry connections for systems 1 (solid) and 2 (dashed), see text and Methods for details. (e) Sideband population beating at Γ for system 1 (solid) and system 2 (dashed). The beating amplitude of system 2 is enhanced 150 times so it is visible on the same scale due to the smaller coupling (blue dashed curve in (d)). (f) Sideband population beating in system 1 for various frequency detunings between harmonic 13 and the energy of the first conduction band at Γ : -0.011 eV in dark blue, -0.0055 eV in light blue, on resonance in grey, 0.0055 eV in light red and 0.011 eV in dark red. (g) RABBIT phase of the beatings in panel (f) as a function of the detuning, extracted from fitting to Eq. 1.

If the relative harmonic phase is known in advance, the RABBIT beating phase records the difference between the phase of the two-photon transition matrix elements ¹⁰ (see Eq. 2 and Methods). For transitions in the bulk of solids, the matrix element between the Bloch state of band m and that of band n at the crystal momentum \mathbf{k} can be written in the length gauge in terms of the position operator,

$$\hat{\mathbf{r}} = i\partial_{\mathbf{k}}\delta_{nm} + \mathbf{A}_{nm\mathbf{k}}. \quad (3)$$

The first term in the RHS can be neglected for weak fields and $\mathbf{A}_{nm\mathbf{k}} = i\langle u_{n\mathbf{k}}|\nabla_{\mathbf{k}}u_{m\mathbf{k}}\rangle$ is the Berry connection, with $u_{n\mathbf{k}}$ the periodic part of the Bloch state of band n . Then, the two-photon matrix element between an initial state in band m and a final state in sideband n at the crystal momentum \mathbf{k} is the two-photon Berry connection (TPBC),

$$A_{nm\mathbf{k},\parallel}^{(2)}(\omega) = \sum_j A_{nj\mathbf{k},\parallel}A_{jm\mathbf{k},\parallel} / [\varepsilon_m(\mathbf{k}) + \omega - \varepsilon_j(\mathbf{k})], \quad (4)$$

where \parallel indicates the component parallel to the laser polarization (we assume all fields linearly polarized along the same direction). The phase recorded by RABBIT is the relative phase between the TPBC,

$$\begin{aligned} \Delta\varphi_{nm\mathbf{k}} = & \arg \left\{ A_{nm\mathbf{k},\parallel}^{(2)}((2N+1)\omega) + A_{nm\mathbf{k},\parallel}^{(2)}(-\omega) \right\} \\ & - \arg \left\{ A_{nm\mathbf{k},\parallel}^{(2)}((2N-1)\omega) + A_{nm\mathbf{k},\parallel}^{(2)}(\omega) \right\}. \end{aligned} \quad (5)$$

This phase allows to extract information on interband dynamics in solids in the same way as it does for photo-ionization dynamics in atoms.

Fig. 2e shows the relative amplitude and phase of the TPBC along the \mathbf{K} - \mathbf{M} direction. The value of the phase at \mathbf{k}_{SB} is exactly $\Delta\varphi = \pi$. Since we fixed the relative phase between the

harmonic pulses to $\Delta\phi = \pi$, the RABBIT signal will oscillate with a phase $\theta = \Delta\phi + \Delta\varphi = 2\pi$, and thus maximize at zero time delay according to Eq. 1. This is what we find in Fig. 2d.

To further demonstrate the sensitivity of the RABBIT beating phase to the phase of the Berry connections, we made simulations on two model systems with exactly the same band structure but with different Berry connections (see Methods for details on the implementation). The band structure is shown in Fig. 3a. At $\mathbf{k}_{\text{SB}} \equiv \Gamma$, a RABBIT measurement can be performed by using a fundamental probe frequency $\omega = 0.172$ a.u. in combination with the pump harmonics 13ω and 15ω . Fig. 3b,c shows the electron momentum distributions of the sideband in one of the systems (system 1) for two time delays separated by half the RABBIT period, clearly showing the different interference pattern at Γ . Similar behaviour is observed for system 2. The relative amplitude and phase of the TPBC are shown in Fig. 3d for system 1 (solid red) and system 2 (dashed red). Their phase differs by π at Γ . Fig. 3e displays the RABBIT beating signal at Γ in the two systems, which appear shifted by π . Note that the band structure and the laser fields are exactly the same for both systems, so that the π difference in the RABBIT phase reflects the π difference in the relative phase of the TPBC (Eq. 5 and Fig. 3d).

One of the most striking examples of the link between the RABBIT beating phase and the phase of the two-photon matrix elements in atoms and molecules is that in which one of the harmonics traverses a bound state^{7,31–35}. In this case, the intermediate step in the two-photon process is dominated by a single resonant state with energy E_{res} , so that the two-photon matrix element $\mathcal{M}_{nm}(\omega) = \mathcal{O}_{nj}\mathcal{O}_{jm}/(E_m + \omega - E_{\text{res}})$ displays a phase shift of π as a function of the detuning of

the frequency ω from the resonance. Provided one can control the detuning of one of the harmonic frequencies with respect to the bound resonant state while keeping the rest of the frequencies unchanged, the RABBIT phase will display a π excursion as the harmonic crosses the resonance³¹. This is in contrast to the case where transitions occur through unstructured continuum states, i.e., far from thresholds and autoionizing states, where the RABBIT phase varies smoothly as a function of energy. We expect the same behaviour for resonant transitions between bands in solids.

For transitions between deep valence bands and high conduction bands (where the bands are finely spaced), we expect that the RABBIT phase varies smoothly as the frequency of one of the harmonics is varied, in similarity to transitions between unstructured continuum states in atoms. However, for transitions between low conduction bands, such as those shown in Fig. 2a and Fig. 3a, we expect that the detuning of one of the harmonics from the intermediate band will lead to a $\sim \pi$ shift of the RABBIT phase.

To prove this, we consider again the model system 1 in Fig. 3. We change the frequency of harmonic H13, while keeping all other field parameters the same; in particular, the frequencies of H15 and the fundamental remain unchanged. Fig. 3f shows the RABBIT beating and phase for various detunings between the central frequency of H13 and the first conduction band at Γ . Far from resonance (dark red and dark blue), the RABBIT beating is small, but one can clearly distinguish a π shift in the oscillation between negatively detuned (dark blue) and positively detuned (dark red) frequencies. To visualize it more clearly, we fit the oscillations to Eq. 1 and extract the phase. Fig. 3g shows the result, where one can observe the π shift as H13 crosses the resonance,

in agreement with Eq. 5. Note that higher/lower detunings than those shown will not generate a RABBIT oscillation since only one quantum path will be dominant.

So far, we have demonstrated how the RABBIT technique can be applied to solids, allowing to extract the same dynamical observables as in atoms or molecules. We have done so assuming no electronic decoherence. There is, however, a fundamental difference between RABBIT in atoms and solids. In atoms, if the pump and the probe pulses do not temporally overlap, radiative transitions between unstructured continuum states are forbidden. In solids, interband transitions are always allowed and there will be a RABBIT beating for non-overlapping pulses as long as there is coherence between the bands.

To study the dependence of the RABBIT beating on electron decoherence, we introduce a dephasing time in model system 1 (Fig. 3). We do so with a phenomenological parameter T_2 that exponentially suppresses the non-diagonal elements of the density matrix (see Methods for further details). In Fig. 4a we show the RABBIT beating of the sideband population at Γ in model system 1 for different dephasing times. The time-delay between the pump and probe pulses is larger than 136 optical cycles (Fig. 4a), guaranteeing no temporal overlap between them. In absence of mechanisms leading to electronic decoherence, i.e., when $T_2 \rightarrow \infty$, the amplitude of the RABBIT beating does not decay with time and remains strong (green curve). Using the same pulse conditions, the beating amplitude is strongly suppressed when $T_2 = 100$ fs (magenta) and it is completely cancelled for $T_2 = 2$ fs (red). Therefore, RABBIT in the limit of non-overlapping pulses offers an opportunity to extract dephasing times.

When dephasing can be well approximated by a constant exponential decay of the coherence, the RABBIT beating amplitude will simply follow the function

$$f(t) = Ae^{-t/T_2} \cos [2\omega t + \theta] + B, \quad (6)$$

where A , B , θ and T_2 are fitting parameters (many of which can be strongly bounded). For more complex decoherence mechanisms, the fitting function may need to include more parameters but the general approach still remains valid. Fig. 4b shows the RABBIT beating in model system 1 with $T_2 = 5$ fs for a wide range of time delays, from perfectly overlapping pulses at $\tau = 0$ fs to non-overlapping at $\tau > 27.5$ fs. As before, the RABBIT signal is computed at Γ . To reduce computational cost, the duration of the pulses in this case was limited to 10 fs full width at half maximum. The field strengths were $F_{15\omega} = 0.005$ V/Å, $F_\omega = 0.01$ V/Å. The beating amplitude starts to decrease at around $\tau = 15$ fs, and follows an exponential decay as a consequence of electronic decoherence. Fitting the beating to Eq. 6 for times where the signal decreases ($\tau > 20$ fs), yields a value of the dephasing parameter of $T_2^{(\text{fit})} = 5.06$ fs, in perfect agreement with the numerical input value. The same fitting procedure is applied in Fig. 4c, where the dephasing parameter was set to $T_2 = 20$ fs, retrieving a fitted value of $T_2^{(\text{fit})} = 18$ fs. For these simulations we have neglected the effect of population relaxation (which will lead to a similar decay of the RABBIT signal) since its timescale is generally much larger than that of dephasing. We note, however, that the decay of the RABBIT signal in solids due to population relaxation should be similar to that observed for the case of transitions through autoionizing atomic states^{33,36}.

In conclusion, we have demonstrated that, with the use of ARPES, the RABBIT technique can be applied to solids and can be used to extract the same dynamical observables as in atomic and

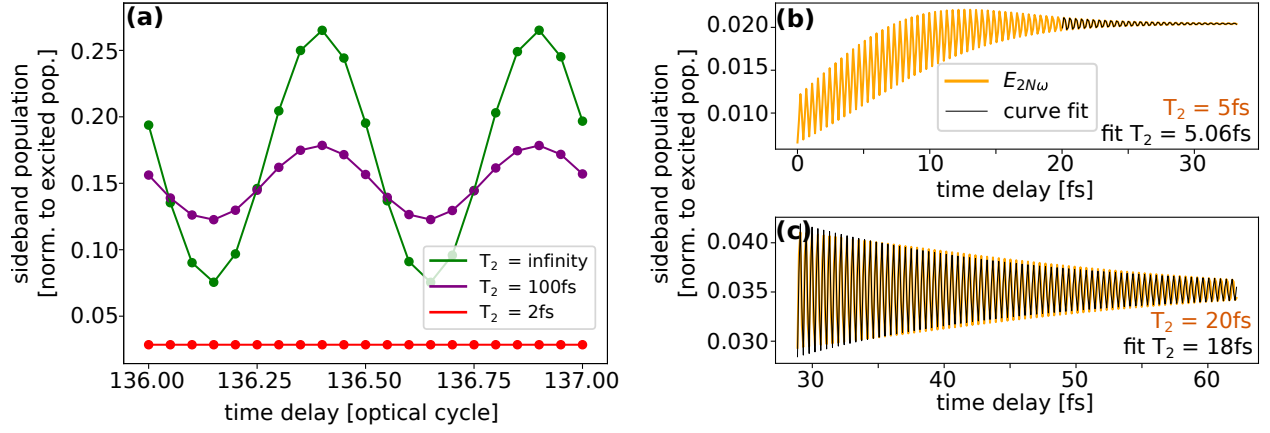


Figure 4: (a) RABBIT signal of model system 1 at Γ for non-overlapping pump and probe pulses. The optical cycle corresponds to $T = 0.88$ fs, see text for other pulse parameters. Three dephasing times are shown: no decoherence (green curve), $T_2 = 100$ fs (purple curve) and $T_2 = 2$ fs (red curve). (b) In orange, the RABBIT signal at Γ for pump-probe time delays τ ranging from perfectly overlapping pulses ($\tau = 0$ fs) to non-overlapping ($\tau > 27.5$ fs). The dephasing time is $T_2 = 5$ fs. In black, the fitting to Eq. 6 for times in which the beating signal is decreasing ($\tau > 20$ fs). (c) Same as panel (b) but for a dephasing time of $T_2 = 20$ fs in the range of time delays where the pulses are always non-overlapping.

molecular targets, opening the way to obtain relative amplitudes and phases of Berry connections, excitation time delays associated with interband transitions and to reconstruct excited electronic wavepackets in the bulk of solids. For high-energy bands, where there is a small energy spacing of the bands at each crystal momenta \mathbf{k} , the usual RABBIT scheme with frequencies $(2N + 1)\omega$, $(2N - 1)\omega$, and ω can be used. For conduction bands close to the bulk band gap, we have shown that it is also possible to find \mathbf{k} -points in which such scheme can be performed with realistic laser frequencies. If phase-locking of four different frequencies is possible, one should be able to probe any band at any region of the Brillouin zone with this method. We anticipate that this method can provide interesting information also on transitions through excitonic states. Also, in contrast to atoms, RABBIT in solids can generate signals at various crystal momenta \mathbf{k} and at various energies with the same pair of consecutive harmonics, in a single shot. This allows to extract dynamical information between states of different energies, e.g., relative time delays between different orbitals, without influence of the relative phase of the harmonics in the comb. Finally, we have shown that the RABBIT signal in solids is extremely sensitive to decoherence mechanisms, providing a simple interferometric way to extract dephasing times.

Methods

Tight-binding model We use a 2D square-lattice model with a unit cell composed of four orbitals. Two of the orbitals (0 and 2) are located at $\mathbf{R} = \mathbf{0}$, while the other two orbitals (1 and 3) are separated by a distance $a = 3.98 \text{ \AA}$, placed in a similar manner to a (100) surface of MgO. The on-site energies are $E_0 = -2.08 \text{ a.u.}$, $E_1 = 0.17 \text{ a.u.}$, $E_2 = 0.35 \text{ a.u.}$ and $E_3 = 0.42 \text{ a.u.}$,

corresponding to the valence band, first, second and third conduction bands, respectively. We included first neighbour hoppings between the orbitals with a fixed hopping parameter of $t = 0.02$ a.u. Higher neighbour hoppings are neglected. Additionally, we include a constant (dipole) coupling between the n and m orbitals in the same unit cell, $\mathbf{r}_{nm,\text{u.c.}} = \langle n|\hat{\mathbf{r}}|m\rangle$, in order to have a strong coupling between bands at the G point. Changing this parameter allows to modify the Berry connections without modifying the band structure. For system 1 we used $\mathbf{r}_{02,\text{u.c.}} = \mathbf{r}_{13,\text{u.c.}} = 0.2$ a.u. and $\mathbf{r}_{03,\text{u.c.}} = \mathbf{r}_{23,\text{u.c.}} = 0$ a.u.. For system 2, $\mathbf{r}_{02,\text{u.c.}} = 0.2$ a.u. and $\mathbf{r}_{13,\text{u.c.}} = \mathbf{r}_{03,\text{u.c.}} = \mathbf{r}_{23,\text{u.c.}} = 0$ a.u..

hBN field-free DFT calculation To obtain the field-free band structure and dipole couplings (Berry connections) of hBN we first perform a DFT calculation with Quantum Espresso³⁷. We use a HSE functional with a 10x10x4 Monkhorst-Pack grid. This gives a minimum band gap of ~ 6 eV, in line with previous works. To achieve a fixed phase relation of the dipole couplings at different k , we transform our basis to the maximally-localized Wannier basis with the Wannier90 suite³⁸. For this, we project onto the p_z and sp_2 orbitals of boron and nitride. In this way, we obtain a tight-binding representation of field-free hBN, which is then propagated using our code³⁹, briefly described below.

Propagation in presence of the field We solve the density matrix equation in the dipole approximation and in the length gauge,

$$\partial_t \rho_{nm}(\mathbf{k}, t) = -i \left[\hat{H}(\mathbf{k}, t), \hat{\rho}(\mathbf{k}, t) \right]_{nm} - \frac{(1 - \delta_{nm}) \rho_{nm}(\mathbf{k}, t)}{T_2} \quad (7)$$

using the code described in³⁹. The Hamiltonian of our system is $H(\mathbf{k}, t) = H_0(\mathbf{k}) + |e|\mathbf{E}(t) \cdot \mathbf{r}$, where H_0 is the periodic field-free tight-binding Hamiltonian constructed as indicated above

and $\mathbf{E}(t)$ is the time-dependent field. The representation of the position operator is that given by Blount⁴⁰, $\hat{\mathbf{r}} = i\partial_{\mathbf{k}} + \hat{\mathbf{A}}(\mathbf{k})$, where $\hat{\mathbf{A}}(\mathbf{k})$ is the Berry connection. Dephasing is introduced in a phenomenological way via the constant dephasing time parameter T_2 , which exponentially suppresses the coherences between the bands. The initial state is a mixed state, with no coherence between the bands, where the valence band is fully occupied and the conduction bands are empty. The final populations are obtained from the diagonal elements of the density matrix at a time when the pulse is over. For the square-lattice model, converged results were obtained with a grid of $n_{k_x} = n_{k_y} = 200$ points and a step size of $dt = 0.025$ a.u.. For monolayer hBN, we used a grid of $n_{k_x} = n_{k_y} = 400$ points and a $dt = 0.1$ a.u..

RABBIT expression The RABBIT protocol is an interference of four time-ordered two-photon paths that reach the same final energy Ω . Since we consider transitions from a low-lying state to a high-lying state, e.g., ground electronic state to continuum or deep valence band to conduction band, we assume that the paths are formed by the absorption of a high frequency pump photon and the absorption or stimulated emission of a probe photon. Let us denote the pump photons by ω_1 and ω'_1 and the probe photons by ω_2 and ω'_2 . The paths interfere at the energy Ω . To reproduce the usual RABBIT implementation, where there are two paths contributing “from above” and two “from below” (Fig. 1a), we take $\Omega = \omega_1 + \omega_2 = \omega'_1 - \omega'_2$, where $+$ corresponds to photon absorption and $-$ to stimulated photon emission; any other combination of frequencies will not contribute to this energy, e.g., $\omega_1 + \omega'_2 \neq \Omega$. Therefore, the paths containing $\omega_1 < \Omega$ contribute “from below” and are associated to ω_2 probe photon absorption while the paths containing $\omega'_1 > \Omega$ contribute “from above” and are associated to ω'_2 probe photon emission. We write the four paths as: (i)

$+\omega_1 + \omega_2$, (ii) $+\omega'_1 - \omega'_2$, (iii) $+\omega_2 + \omega_1$, (iv) $-\omega'_2 + \omega'_1$, as shown in Fig. 1a. The first frequency is absorbed/emitted first.

Let us consider path (i), where we first absorb the pump photon ω_1 , and then absorb the probe photon ω_2 . We assume monochromatic pulses, so that for the pump field we have

$$F_{\omega_1}(t) = F_{0,\omega_1} \cos(\omega_1 t + \phi_{\omega_1}) = \frac{F_{0,\omega_1}}{2} (e^{i\phi_{\omega_1}} e^{i\omega_1 t} + e^{-i\phi_{\omega_1}} e^{-i\omega_1 t}). \quad (8)$$

The probe field is delayed by a time τ , so that

$$F_{\omega_2}(t) = \frac{F_{0,\omega_2}}{2} (e^{i(\phi_{\omega_2} + \omega_2 \tau)} e^{i\omega_2 t} + e^{-i(\phi_{\omega_2} + \omega_2 \tau)} e^{-i\omega_2 t}). \quad (9)$$

The second order amplitude in the Dyson expansion is

$$\mathcal{A}_{fi}^{(2)} = - \sum_j \mathcal{O}_{fj} \mathcal{O}_{ji} \int_{t_0}^t dt_1 e^{iE_{fj}t_1} F(t_1) \int_{t_0}^{t_1} dt_2 e^{iE_{ji}t_2} F(t_2), \quad (10)$$

where the \mathcal{O}_{ba} are the transition matrix elements, e.g., in length gauge $\mathcal{O}_{ba} = \langle b|\mathbf{r}|a\rangle$. For monochromatic pulses, we can compute the amplitude taking $t_0 \rightarrow -\infty$ and $t \rightarrow +\infty$. Then,

$$\mathcal{A}_{fi,(i)}^{(2)} = - \frac{F_{0,\omega_2} e^{-i(\phi_{\omega_2} + \omega_2 \tau)}}{2} \frac{F_{0,\omega_1} e^{-i\phi_{\omega_1}}}{2} \sum_j \mathcal{O}_{fj} \mathcal{O}_{ji} \int_{-\infty}^{\infty} dt_1 e^{i(E_{fj} - \omega_2)t_1} \int_{-\infty}^{t_1} dt_2 e^{i(E_{ji} - \omega_1)t_2}, \quad (11)$$

where subscript (i) indicates which path we consider. The second integral in Eq. 11 can be solved by introducing a decaying exponential in the limit of $t \rightarrow \infty$,

$$\int_{-\infty}^t d\tau e^{i\omega\tau} \rightarrow \lim_{\nu \rightarrow 0^+} \int_{-\infty}^t dt_1 e^{i(\omega - i\nu)t_1} = i \frac{e^{i\omega t}}{-\omega + i0^+}, \quad (12)$$

where $(x + i0^+)^{-1}$ is a distribution. Using Eq. 12 in the second integral of Eq. 11,

$$\mathcal{A}_{fi,(i)}^{(2)} = -i \frac{F_{0,\omega_2} e^{-i(\phi_{\omega_2} + \omega_2 \tau)}}{2} \frac{F_{0,\omega_1} e^{-i\phi_{\omega_1}}}{2} \sum_j \frac{\mathcal{O}_{fj} \mathcal{O}_{ji}}{E_i + \omega_1 - E_j + i0^+} \int_{-\infty}^{\infty} dt_1 e^{i(E_{fi} - \omega_1 - \omega_2)t_1}. \quad (13)$$

We identify the integral with the delta distribution, i.e., $\int_{-\infty}^{\infty} dt e^{i(\omega-\omega_0)t} = 2\pi\delta(\omega - \omega_0)$, so that

$$\mathcal{A}_{fi,(i)}^{(2)} = -2\pi i \frac{F_{0,\omega_2} e^{-i(\phi_{\omega_2} + \omega_2\tau)}}{2} \frac{F_{0,\omega_1} e^{-i\phi_{\omega_1}}}{2} \sum_j \frac{\mathcal{O}_{fj} \mathcal{O}_{ji}}{E_i + \omega_1 - E_j + i0^+} \delta(E_{fi} - \omega_1 - \omega_2). \quad (14)$$

For compactness, let us write the two-photon transition matrix element as

$$\mathcal{M}_{fi}(\omega_1) = \sum_j \frac{\mathcal{O}_{fj} \mathcal{O}_{ji}}{E_i + \omega_1 - E_j + i0^+}. \quad (15)$$

Then, the transition amplitude reads,

$$\mathcal{A}_{fi,(i)}^{(2)} = -2\pi i \frac{F_{0,\omega_2} e^{-i(\phi_{\omega_2} + \omega_2\tau)}}{2} \frac{F_{0,\omega_1} e^{-i\phi_{\omega_1}}}{2} \mathcal{M}_{fi}(\omega_1) \delta(E_{fi} - \Omega), \quad (16)$$

where $\Omega = \omega_1 + \omega_2 = \omega'_1 - \omega'_2$ is the sideband energy. The other three paths contributing to the RABBIT signal follow,

$$\mathcal{A}_{fi,(ii)}^{(2)} = -2\pi i \frac{F_{0,\omega'_2} e^{i(\phi_{\omega'_2} + \omega'_2\tau)}}{2} \frac{F_{0,\omega'_1} e^{-i\phi_{\omega'_1}}}{2} \mathcal{M}_{fi}(\omega'_1) \delta(E_{fi} - \Omega), \quad (17)$$

$$\mathcal{A}_{fi,(iii)}^{(2)} = -2\pi i \frac{F_{0,\omega_2} e^{-i(\phi_{\omega_2} + \omega_2\tau)}}{2} \frac{F_{0,\omega_1} e^{-i\phi_{\omega_1}}}{2} \mathcal{M}_{fi}(\omega_2) \delta(E_{fi} - \Omega), \quad (18)$$

$$\mathcal{A}_{fi,(iv)}^{(2)} = -2\pi i \frac{F_{0,\omega'_2} e^{i(\phi_{\omega'_2} + \omega'_2\tau)}}{2} \frac{F_{0,\omega'_1} e^{-i\phi_{\omega'_1}}}{2} \mathcal{M}_{fi}(-\omega'_2) \delta(E_{fi} - \Omega), \quad (19)$$

For brevity, we group paths (i) and (iii) on the one hand, and paths (ii) and (iv) on the other, which correspond, respectively, to absorption of an ω_2 photon and stimulated emission of an ω'_2 probe photon,

$$\mathcal{A}_{fi,\text{em}}^{(2)} = -2\pi i \frac{F_{0,\omega_2} e^{-i(\phi_{\omega_2} + \omega_2\tau)}}{2} \frac{F_{0,\omega_1} e^{-i\phi_{\omega_1}}}{2} [\mathcal{M}_{fi}(\omega_1) + \mathcal{M}_{fi}(\omega_2)] \delta(E_{fi} - \Omega). \quad (20)$$

$$\mathcal{A}_{fi,\text{abs}}^{(2)} = -2\pi i \frac{F_{0,\omega'_2} e^{i(\phi_{\omega'_2} + \omega'_2\tau)}}{2} \frac{F_{0,\omega'_1} e^{-i\phi_{\omega'_1}}}{2} [\mathcal{M}_{fi}(\omega'_1) + \mathcal{M}_{fi}(-\omega'_2)] \delta(E_{fi} - \Omega). \quad (21)$$

The total intensity at the sideband energy is the coherent sum of Eq. 20 and Eq. 21,

$$\begin{aligned}
I_{\text{SB}} &= |\mathcal{A}_{f_i, \text{abs}}^{(2)} + \mathcal{A}_{f_i, \text{em}}^{(2)}|^2 \\
&= \frac{\pi^2}{4} \left\{ |F_{0, \omega_1}|^2 |F_{0, \omega_2}|^2 |\mathcal{M}_{f_i}(\omega_1) + \mathcal{M}_{f_i}(\omega_2)|^2 \right. \\
&\quad + |F_{0, \omega'_1}|^2 |F_{0, \omega'_2}|^2 |\mathcal{M}_{f_i}(\omega'_1) + \mathcal{M}_{f_i}(-\omega'_2)|^2 \\
&\quad + 2|F_{0, \omega_1} F_{0, \omega_2} [\mathcal{M}_{f_i}(\omega_1) + \mathcal{M}_{f_i}(\omega_2)] F_{0, \omega'_1} F_{0, \omega'_2} [\mathcal{M}_{f_i}(\omega'_1) + \mathcal{M}_{f_i}(-\omega'_2)]| \\
&\quad \left. \times \cos(\phi_{\omega'_1} - \phi_{\omega_1} - (\phi_{\omega_2} + \phi_{\omega'_2}) + \varphi_{\text{abs}} - \varphi_{\text{em}} - (\omega_2 + \omega'_2)\tau) \right\}, \tag{22}
\end{aligned}$$

where we have defined the atomic phases

$$\varphi_{\text{abs}} = \arg[\mathcal{M}_{f_i}(\omega_1) + \mathcal{M}_{f_i}(\omega_2)], \quad \varphi_{\text{em}} = \arg[\mathcal{M}_{f_i}(\omega'_1) + \mathcal{M}_{f_i}(-\omega'_2)]. \tag{23}$$

For the case in which the probe frequencies are the same $\omega_2 = \omega'_2 = \omega$, and the pump frequencies are odd harmonics of the probe, $\omega_1 = (2N - 1)\omega$ and $\omega'_1 = (2N + 1)\omega$, Eq. 22 and Eq. 23 reduce to Eq. 1 and Eq. 2.

1. Goulielmakis, E. *et al.* Attosecond control and measurement: lightwave electronics. *Science* **317**, 769–775 (2007).
2. Krausz, F. & Ivanov, M. Attosecond physics. *Rev. Mod. Phys.* **81**, 163–234 (2009).
3. Vénier, V., Taïeb, R. & Maquet, A. Phase dependence of (N+1)-color (N_i1) ir-uv photoionization of atoms with higher harmonics. *Phys. Rev. A* **54**, 721–728 (1996). URL <https://link.aps.org/doi/10.1103/PhysRevA.54.721>.

4. Muller, H. G. Reconstruction of attosecond harmonic beating by interference of two-photon transitions. *Applied Physics B* **74**, s17–s21 (2002). URL <https://doi.org/10.1007/s00340-002-0894-8>.
5. Paul, P. M. *et al.* Observation of a train of attosecond pulses from high harmonic generation. *Science (New York, N.Y.)* **292**, 1689–92 (2001). URL <http://www.ncbi.nlm.nih.gov/pubmed/11387467>.
6. Klünder, K. *et al.* Probing Single-Photon Ionization on the Attosecond Time Scale. *Phys. Rev. Lett.* **106**, 143002 (2011).
7. Gruson, V. *et al.* Attosecond dynamics through a Fano resonance: Monitoring the birth of a photoelectron. *Science* **354** (2016). URL <http://science.sciencemag.org/content/354/6313/734>.
8. Donsa, S., Douguet, N., Burgdörfer, J., Březinová, I. & Argenti, L. Circular Holographic Ionization-Phase Meter. *Phys. Rev. Lett.* **123**, 133203 (2019). URL <https://link.aps.org/doi/10.1103/PhysRevLett.123.133203>.
9. Jiménez-Galán, Á., Martín, F. & Argenti, L. Two-photon finite-pulse model for resonant transitions in attosecond experiments. *Physical Review A* **93** (2016). URL <https://link.aps.org/doi/10.1103/PhysRevA.93.023429>.
10. Dahlström, J. M. *et al.* Theory of attosecond delays in laser-assisted photoionization. *Chemical Physics* 1–12 (2012). URL <http://linkinghub.elsevier.com/retrieve/pii/S0301010412000298>.

11. Pazourek, R., Nagele, S. & Burgdörfer, J. Attosecond chronoscopy of photoemission. *Rev. Mod. Phys.* **87**, 765–802 (2015). URL <https://link.aps.org/doi/10.1103/RevModPhys.87.765>.
12. Isinger, M. *et al.* Photoionization in the time and frequency domain. *Science* **358**, 893–896 (2017). URL <https://science.sciencemag.org/content/358/6365/893>.
13. Argenti, L. *et al.* Control of photoemission delay in resonant two-photon transitions. *Phys. Rev. A* **95**, 43426 (2017). URL <https://link.aps.org/doi/10.1103/PhysRevA.95.043426>.
14. Vos, J. *et al.* Orientation-dependent stereo Wigner time delay and electron localization in a small molecule. *Science* **360**, 1326–1330 (2018). URL <https://science.sciencemag.org/content/360/6395/1326>.
15. Busto, D. *et al.* Time–frequency representation of autoionization dynamics in helium. *Journal of Physics B: Atomic, Molecular and Optical Physics* **51**, 44002 (2018). URL <https://doi.org/10.1088%2F1361-6455%2F51%2F44002>.
16. Kruchinin, S. Y., Krausz, F. & Yakovlev, V. S. Colloquium: Strong-field phenomena in periodic systems. *Rev. Mod. Phys.* **90**, 21002 (2018). URL <https://link.aps.org/doi/10.1103/RevModPhys.90.021002>.
17. Ghimire, S. *et al.* Observation of high-order harmonic generation in a bulk crystal. *Nature Physics* **7**, 138–141 (2011). URL <http://www.nature.com/nphys/journal/v7/>

n2/full/nphys1847.html%5Cnhttp://www.nature.com/nphys/journal/v7/n2/pdf/nphys1847.pdf.

18. Langer, F. *et al.* Lightwave valleytronics in a monolayer of tungsten diselenide. *Nature* **557**, 76–80 (2018). URL <https://doi.org/10.1038/s41586-018-0013-6>.
19. Cavalieri, A. L. *et al.* Attosecond spectroscopy in condensed matter. *Nature* **449**, 1029–1032 (2007).
20. Garg, M. *et al.* Multi-petahertz electronic metrology. *Nature* **538** (2016). URL <http://dx.doi.org/10.1038/nature19821>.
21. Moulet, A. *et al.* Soft x-ray excitonics. *Science* **357**, 1134–1138 (2017). URL <https://science.sciencemag.org/content/357/6356/1134>.
22. Buades, B. *et al.* Attosecond-resolved petahertz carrier motion in semi-metallic TiS₂. *arXiv:1808.06493* (2018).
23. Lakhotia, H. *et al.* Laser picoscopy of valence electrons in solids. *Nature* **583**, 55–59 (2020). URL <https://doi.org/10.1038/s41586-020-2429-z>.
24. Silva, R. E. F., Blinov, I. V., Rubtsov, A. N., Smirnova, O. & Ivanov, M. High-harmonic spectroscopy of ultrafast many-body dynamics in strongly correlated systems. *Nature Photonics* **12**, 266–270 (2018). URL <https://doi.org/10.1038/s41566-018-0129-0>.

25. Bauer, D. & Hansen, K. K. High-Harmonic Generation in Solids with and without Topological Edge States. *Phys. Rev. Lett.* **120**, 177401 (2018). URL <https://link.aps.org/doi/10.1103/PhysRevLett.120.177401>.
26. Silva, R. E. F., Jiménez-Galán, Á., Amorim, B., Smirnova, O. & Ivanov, M. Topological strong-field physics on sub-laser-cycle timescale. *Nature Photonics* (2019). URL <https://doi.org/10.1038/s41566-019-0516-1>.
27. Seiffert, L. *et al.* Attosecond chronoscopy of electron scattering in dielectric nanoparticles. *Nature Physics* **13**, 766–770 (2017). URL <https://doi.org/10.1038/nphys4129>.
28. Jiménez-Galán, Á., Silva, R. E., Smirnova, O. & Ivanov, M. Y. Lightwave topology for strong-field valleytronics. *arXiv:1910.07398* (2019).
29. Locher, R. *et al.* Energy-dependent photoemission delays from noble metal surfaces by attosecond interferometry. *Optica* **2**, 405–410 (2015). URL <http://www.osapublishing.org/optica/abstract.cfm?URI=optica-2-5-405>.
30. Ambrosio, M. J. & Thumm, U. Energy-resolved attosecond interferometric photoemission from Ag(111) and Au(111) surfaces. *Phys. Rev. A* **97**, 43431 (2018). URL <https://link.aps.org/doi/10.1103/PhysRevA.97.043431>.
31. Swoboda, M. *et al.* Phase Measurement of Resonant Two-Photon Ionization in Helium. *Phys. Rev. Lett.* **104**, 12–15 (2010).
32. Caillat, J. *et al.* Attosecond Resolved Electron Release in Two-Color Near-Threshold Photoionization of N₂. *Phys. Rev. Lett.* **106**, 093002 (2011).

33. Jiménez-Galán, Á., Argenti, L. & Martín, F. Modulation of Attosecond Beating in Resonant Two-Photon Ionization. *Physical Review Letters* **113** (2014). URL <https://link.aps.org/doi/10.1103/PhysRevLett.113.263001>.
34. Kotur, M. *et al.* Spectral phase measurement of a Fano resonance using tunable attosecond pulses. *Nature Communications* **7**, 10566 (2016). URL <https://doi.org/10.1038/ncomms10566>.
35. Cirelli, C. *et al.* Anisotropic photoemission time delays close to a Fano resonance. *Nature Communications* **9**, 955 (2018). URL <https://doi.org/10.1038/s41467-018-03009-1>.
36. Silva, R. E. F., Rivière, P. & Martín, F. Autoionizing decay of h_2 doubly excited states by using xuv-pump–infrared-probe schemes with trains of attosecond pulses. *Phys. Rev. A* **85**, 063414 (2012). URL <https://link.aps.org/doi/10.1103/PhysRevA.85.063414>.
37. Giannozzi, P. *et al.* QUANTUM ESPRESSO: a modular and open-source software project for quantum simulations of materials. *Journal of Physics: Condensed Matter* **21**, 395502 (2009). URL <http://stacks.iop.org/0953-8984/21/i=39/a=395502>.
38. Marzari, N., Mostofi, A. A., Yates, J. R., Souza, I. & Vanderbilt, D. Maximally localized Wannier functions: Theory and applications. *Rev. Mod. Phys.* **84**, 1419–1475 (2012). URL <https://link.aps.org/doi/10.1103/RevModPhys.84.1419>.

39. Silva, R. E. F., Martín, F. & Ivanov, M. High harmonic generation in crystals using maximally localized Wannier functions. *Phys. Rev. B* **100**, 195201 (2019). URL <https://link.aps.org/doi/10.1103/PhysRevB.100.195201>.
40. Blount, E. I. Formalisms of Band Theory. vol. 13, 305–373 (Academic Press, 1962). URL <http://www.sciencedirect.com/science/article/pii/S0081194708604592>.